

## **Relationship between High-Impact Weather Events in Japan and Propagation of Rossby Waves along the Asian Jet in July 2004**

**Takeshi ENOMOTO**

*Earth Simulator Center, Japan Agency for Marine-Earth Science and Technology*

**Hirokazu ENDO**

*Meteorological Research Institute, Japan Meteorological Agency*

**Yayoi HARADA**

*Climate Prediction Division, Japan Meteorological Agency*

**and**

**Wataru OHFUCHI**

*Earth Simulator Center, Japan Agency for Marine-Earth Science and Technology*

*(Manuscript received 5 April 2007, in final form 12 November 2008)*

### **Abstract**

In July 2004, torrential rainfalls caused significant damages in parts of Japan, followed by heat waves. Our data analysis shows that both rainfall and heat wave events in late Baiu season were caused by the intensification of the subtropical anticyclone near Japan (Bonin high) and that intensity of the Bonin high was significantly influenced by propagation of Rossby waves along the subtropical jet. Hindcast experiments from 15 July were conducted to study the mechanisms and predictability of these high-impact weather events. On 17–18 July, localized rainfalls at a few locations along the coast of the Sea of Japan including Sakata and Fukui were successfully simulated in a high-resolution (21-km mesh) global hindcast simulation. These rainfall events were found to occur near the leading edge of a filament of moist and warm air advected clockwise. On 20 July, anomalously high temperature was reproduced in the high-resolution hindcast simulation. With a moderate resolution of 83 km, the intensification of the subtropical anticyclone was reproduced although the föhn was much weaker. This result indicates that temperature distribution associated with föhn requires a resolution high enough to resolve major mountains. In order to investigate the predictability of propagation of Rossby waves and intensification of the Bonin high, 25-member ensemble experiments from 1 July 2004 were conducted using the moderate-resolution model. It is shown that the region along the Asian jet has twice as long predictability as the entire Northern Hemisphere. This case study suggests that the intensification of the Bonin high associated with the propagation of Rossby waves along the Asian jet could be predicted a few weeks in advance with an ensemble forecast at a moderate resolution.

---

Corresponding author: Earth Simulator Center, Japan Agency for Marine-Earth Science and Technology, 3173-25 Showa-machi, Kanazawa-ku, Yokohama, Kanagawa, 236-0001, Japan.  
E-mail: eno@jamstec.go.jp  
© 2009, Meteorological Society of Japan

### **1. High-impact weather events in July 2004**

In July 2004, many parts of Japan were affected by heavy precipitation. For example, the monthly precipitation at Sakata in July (Fig. 1, Letter A in

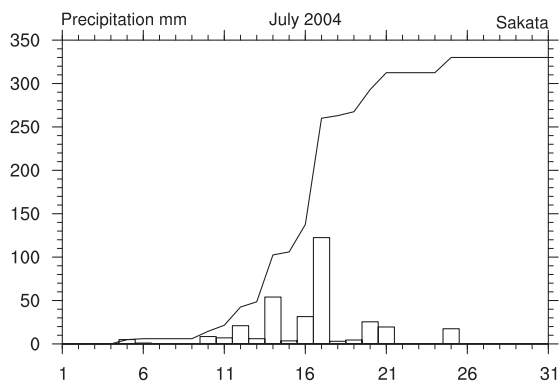


Fig. 1. Daily and accumulated precipitation (mm) in Sakata, in bars and a curve, respectively. The location of Sakata is marked with letter A in Fig. 3. Produced from the JMA AMeDAS data.

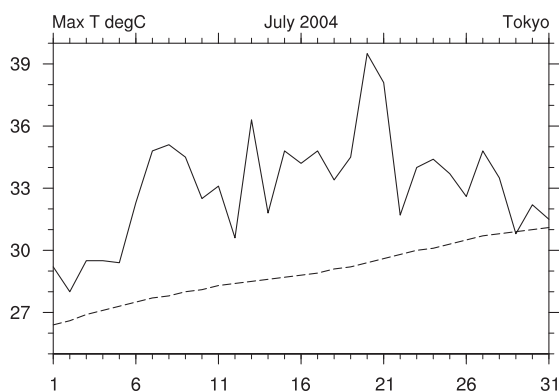


Fig. 2. Daily maximum temperature ( $^{\circ}\text{C}$ ) in Tokyo. The solid and dashed curves represent values for 2004 and for the 30-year average between 1971 and 2000. The location of Tokyo is marked as D in Fig. 3. Produced from the JMA AMeDAS data.

Fig. 3) was 330.0 mm, 177.3% of the climatological value of 186.1 mm according to the Automated Meteorological Data Acquisition System (AMeDAS) data of the Japan Meteorological Agency (JMA). During 12–13 July, the Baiu front was activated and caused torrential rainfall in Niigata and Fukushima. Another event occurred during 17–18 July in Fukui and Sakata due to the activated Baiu front.

High temperature was another feature of that month. Figure 2 shows the daily maximum temperature in Tokyo (Letter D in Fig. 3) in July 2004.

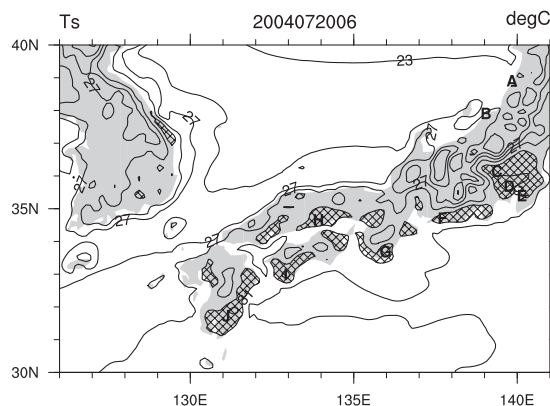


Fig. 3. Distribution of the 2-m temperature ( $^{\circ}\text{C}$ ) near Japan at 6 UTC on 20 July, 2004. Contours are drawn every 2 degrees between  $21^{\circ}\text{C}$  and  $35^{\circ}\text{C}$  and regions with temperature higher than  $31^{\circ}\text{C}$  are hatched. Letters A–J represent observational stations (See Table 1). Produced from the JMA MSM data.

Everyday except for 29 July, the observed maxima exceeded the climatological values. On 20 July, the maximum temperature was a record-breaking value of  $39.5^{\circ}\text{C}$ ,  $10.1^{\circ}\text{C}$  above normal. Anomalously high temperature was not limited to Tokyo. In fact, the highest temperature of  $40.2^{\circ}\text{C}$  was recorded at the AMeDAS station in Ushiku (Letter E in Fig. 3). Figure 3, produced from the meso-scale analysis for the JMA Mesoscale Model (MSM), shows the distribution of the 2-m temperature at 6 UTC (15 JST). The horizontal resolution of MSM is 10 km and the resolution of distributed MSM data at the surface level is  $0.125^{\circ}$  and  $0.1^{\circ}$  in zonal and meridional directions. Although analyzed temperature is cooler by  $1.3$  to  $6.4^{\circ}\text{C}$  than that from AMeDAS observations at selected stations (Table 1), its distribution clearly shows that regions with high temperature are located along the southern coast of Japanese islands and the east coast of the Korean Peninsula. The distributions of temperature (Fig. 3), winds (Fig. 4) and relative humidity (not shown) imply föhn. In fact, the regions with high temperature (hatched in Fig. 3) coincide well with those with low relative humidity (not shown). Possible causes of anomalously high temperature will be discussed further in Subsection 3.4 with hindcasts with two different horizontal resolutions.

In July 2004, the Bonin high was anomalously enhanced as represented by large values ( $>240$  K)

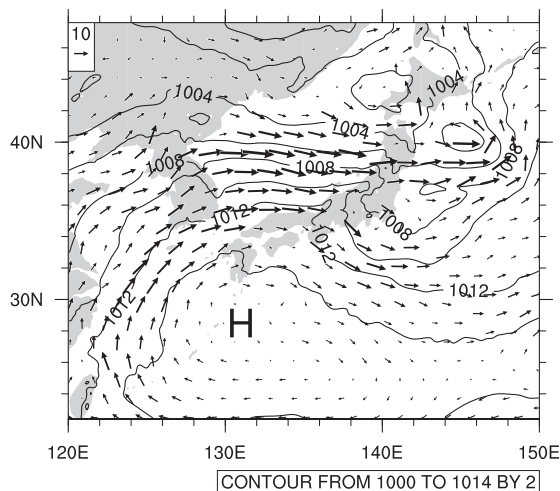


Fig. 4. Distribution of winds ( $\text{m s}^{-1}$ ) at the 925 hPa surface and sea-level pressure near Japan at 6 UTC on 20 July, 2004. Contours are drawn every 2 hPa. Letter H denotes the approximate centre of the anticyclone. Produced from the JMA MSM data.

of out-going long-wave radiation (OLR) in the southwestern Japan (Fig. 5a). In the climatology (Fig. 5b), the convection along the Baiu frontal zone (BFZ) resulted in relatively low OLR. Convection was inactive along BFZ and in the Philippine Sea and active in southern China near  $110^\circ\text{E}$ ,  $20^\circ\text{N}$  (Fig. 5c). Nitta (1987) found that the convection along the BFZ was suppressed when the convection in the Phillipine Sea was enhanced (the PJ pattern). Obviously it was not the case for this month. Recently, a mechanism of intensification of the Bonin high by a mid-latitude process was proposed by Enomoto et al. (2003). They argue that as a result of propagation of Rossby waves along the subtropical jet over Eurasia (the Silk Road pattern), an equivalent barotropic anticyclone is formed over Japan.

There are two wave-guides over Eurasia during the Northern Hemisphere summer: the subpolar and subtropical jets. Intensity and frequency of propagation of Rossby wave-packets along these jets have large impacts on the summer climate near Japan. Rossby waves along the subpolar and subtropical jets intensify the Okhotsk (Nakamura and Fukamachi 2004) and Bonin (Enomoto et al. 2003; Enomoto 2004; Sato and Takahashi 2006) anticyclones, respectively. In 2003, the Rossby-wave

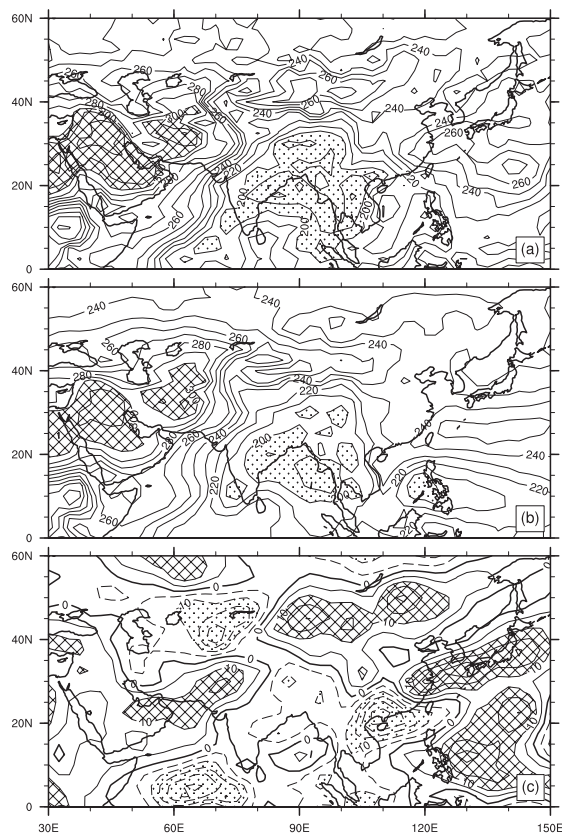


Fig. 5. Distribution of the Out-going Long-wave Radiation ( $\text{W m}^{-2}$ ) of (a) July 2004, (b) the monthly climatology (1979–1995), and (c) the difference ((a)–(b)). Contours are drawn every 10 (Panels a, b) and 5 (Panel c)  $\text{W m}^{-2}$ . Negative contours are broken. Hatched and dotted regions indicate values larger than  $300 \text{ W m}^{-2}$  and smaller than  $200 \text{ W m}^{-2}$ , respectively for Panels a and b. For Panel c, positive and negative out-going long-wave radiation (OLR) anomalies larger than  $10 \text{ W m}^{-2}$  and smaller than  $-10 \text{ W m}^{-2}$  are hatched and dotted, respectively. Produced from the National Oceanic and Atmospheric Administration (NOAA) interpolated OLR dataset.

propagation along the subpolar jet was very active and the propagation along the subtropical jet was weak to the east of  $90^\circ\text{E}$ . As a result, the Okhotsk anticyclone was intense while the Bonin anticyclone did not develop well. In 2004, by contrast, the subpolar propagation was very weak and the Okhotsk high did not develop well (Harada et al. 2006).

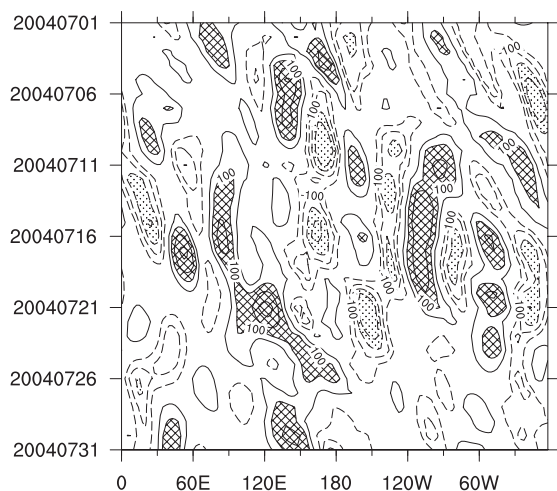


Fig. 6. Longitude-Time cross-section of zonally asymmetric component of the 200 hPa height (gpm) averaged between 35–50°N in July 2004. Anomalies smaller than –100 gpm and larger than 100 gpm are dotted and hatched, respectively. Produced from the NCEP/NCAR reanalysis.

The climatological Rossby wave sources of the Silk Road pattern suggested by Enomoto et al. (2003) are due to the descent caused by the monsoon heating (the monsoon-desert mechanism, Rodwell and Hoskins 1996). According to this mechanism, the contrast between monsoon and desert represents the strength of the monsoon. In July 2004, there was a sharper gradient of OLR near 70°E (Fig. 5a) due to positive anomalies extending from the Arabian Peninsula to Afghanistan with a maximum near 70°E, 30°N and negative anomalies extending from India to southern China with a minimum near 110°E, 20°N (Fig. 5c). This enhanced contrast might have acted as a favourable basic field for the Silk Road pattern and intensification of the Bonin high without active convection in the Philippine Sea.

A time-longitude plot of the geopotential height at 200 hPa (Fig. 6) produced from the National Centers for Environmental Prediction/National Center for Atmospheric Research (NCEP/NCAR) reanalysis (Kalnay et al. 1996) indicates that there were a few events of Rossby wave-packet propagation in July 2004. One of those packets propagated around the globe and intensified the Bonin high in early and late July. Another event initiating on 16 July from 25°E caused the intensification of the Bonin high during 19–21 July near 120°E.

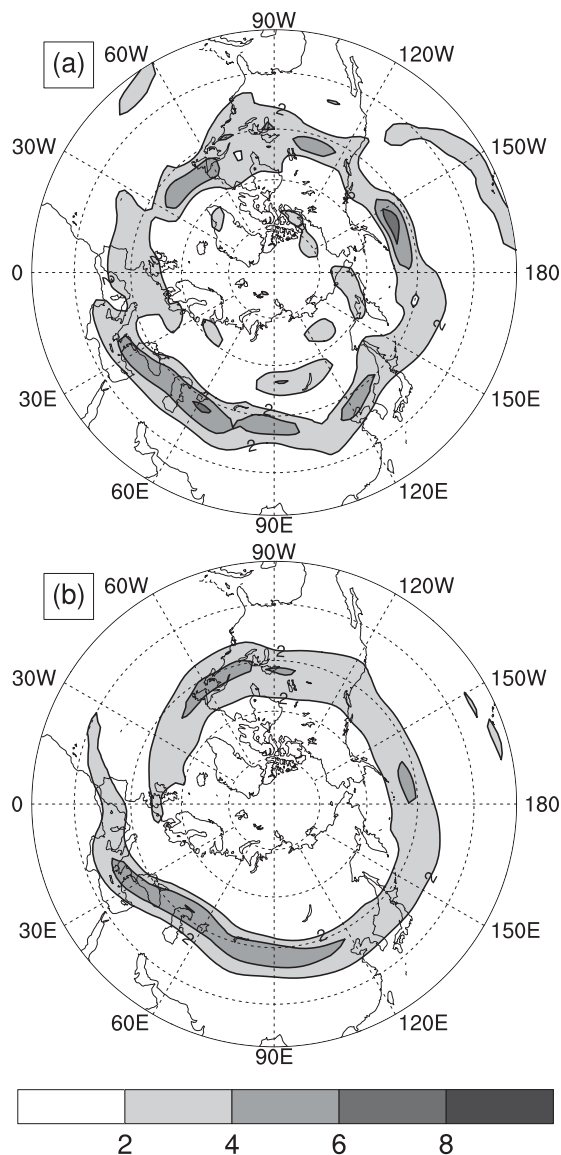


Fig. 7. Distribution of the meridional gradient of the potential vorticity at the 200-hPa ( $10^{-6}$  PVU  $m^{-1} = 10^{-12}$  K m  $kg^{-1}s^{-1}$ ) of (a) July 2004, (b) the monthly climatology (1968–1996). Produced from the NCEP/NCAR reanalysis.

The basic flows provide insights into the reasons why Rossby-wave propagation took place along the subtropical jet rather than the subpolar jet in July 2004. There is a well-defined wave-guide represented by the large meridional gradient of potential vorticity (PV) near 40°N over Eurasia (Fig. 7). Its intensity was not particularly different from the

climatological value in terms of the meridional gradient of the monthly-mean PV. However, there are a few distinctive features. 1) The North Atlantic wave-guide is connected to the subtropical jet over Eurasia, as indicated by a larger meridional PV gradient near 10°W, 45°N. In the climatology, it is connected to the subpolar wave-guide. In some years such as in 2003, Rossby-wave propagation was active along the subpolar jet. In July 2004, due to an easterly region at the 300-hPa surface over northern Europe, the energy propagation of Rossby waves along the subpolar jet was suppressed (not shown). 2) The subtropical jet is split near 90°E as indicated by an enhanced PV gradient extending northeastward. These split jets imply large amplitudes of Rossby waves. 3) A maximum of the PV gradient near Japan is formed. This anomaly can be interpreted as the results of breaking of Rossby waves since anticyclonic breakings bring low PV poleward and reinforce the meridional gradient to their north.

Figure 8 shows the time-averaged upper and lower tropospheric flow patterns during an event in 17–21 July. The undulation of the northern edge of

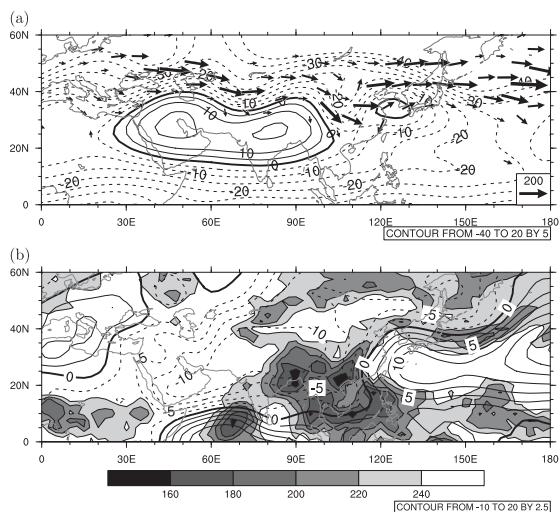


Fig. 8. Distributions of (a) the stream function ( $\times 10^6 \text{ m}^2 \text{ s}$ , contour) and wave activity flux ( $\text{m}^2 \text{ s}^{-2}$ , arrows) at the 200-hPa surface (b) the stream function ( $\times 10^6 \text{ m}^2 \text{ s}$ , contour) at the 850-hPa surface and outgoing long-wave radiation ( $\text{W m}^{-2}$ , shade) averaged in 17–21 July 2004. Produced from the NCEP/NCAR reanalysis and NOAA interpolated OLR.

the Tibetan high and eastward wave activity flux (Takaya and Nakamura 2001) indicate the propagation of Rossby waves (Fig. 8a). In the calculation of the wave activity flux, the 31-day running average is used as the zonally-varying basic flow. In addition to the two centres within the Tibetan high, another anticyclonic centre is created over the East China Sea in the upper troposphere. The wave activity downstream of this high implies a reflection (or an over-reflection). This anticyclone is mainly equivalent-barotropic, although the surface centre is located slightly southeast of the upper-tropospheric centre. Convection is suppressed inside the high but activated along its fringe (Fig. 8b).

The main purpose of this paper is to study the mechanisms and predictability of high-impact weather events that affected Japan in July 2004, described above, as global to regional phenomena. Hindcast simulations at high and moderate resolutions and ensemble experiments at a moderate resolution were conducted using an atmospheric general circulation model (AGCM) described in Section 2. In Section 3, the results from the high-resolution hindcast are examined. The high-resolution simulation seems to capture the precipitation in Sakata and Fukui and temperature distributions associated with the föhn in many parts along the Pacific coast of Japan. Dependency on horizontal resolution, representation of the föhn in particular, is compared between high- and moderate-resolution hindcasts. In Section 4, to investigate the predictability of the subtropical jet in July 2004, the results of ensemble experiments from 1 July for one month with different surface boundary conditions are examined. Finally, the summary and remarks are given in Section 5.

## 2. Model description

AFES (AGCM for the Earth Simulator) is used in this study to enable efficient high-resolution global simulations on the Earth Simulator. It is a global atmospheric model based on Numaguti et al. (1997) but rewritten in Fortran 90 and highly optimized for the Earth Simulator (Shingu et al. 2002, 2003). AFES enables global simulations at high-resolution simulations; up to a 10-km mesh has been tested (Ohfuchi et al. 2004). AFES's dynamical framework employs the pseudo-spectral method with a triangular truncation for the horizontal discretization (Hoskins and Simmons 1975) except that Arakawa and Suarez (1983) discretization is used in the vertical. It has full physical packages in-

cluding statistical grid condensation (Le Treut and Li 1991) and precipitation (Sundqvist 1978), radiation (Nakajima and Tanaka 1986; Nakajima et al. 2000), level-2 moist vertical diffusion (Mellor and Yamada 1982; Smith 1990), and surface flux (Loius 1979; Uno et al. 1995) inherited from Numaguti et al. (1997). There are some changes to the model physics from Numaguti et al. (1997). One of the most significant differences is the use of Emanuel convective scheme (Emanuel 1991; Emanuel and Živković-Rothman 1999; Peng et al. 2004). The cloud model of the Emanuel scheme parametrizes  $O(100\text{ m})$  drafts rather than ensemble of clouds and does not have parameters that depend explicitly on the horizontal resolution. This feature motivated us to incorporate it in AFES (Enomoto et al. 2008).

AFES is used for both hindcast and ensemble simulations. In hindcast simulations from 15 July, high (T639L48) and moderate (T159L48) horizontal resolutions are used to compare the representation of high impact weather events between the two resolutions. The figure after letter 'T' denotes the total truncation wave number and the figure after letter 'L' denotes the number of the model levels. Horizontal grid intervals for high and moderate resolutions are about 21 and 83 km, respectively. In 25-member ensemble experiments, T159L48 is used since propagation of the Rossby waves and enhancement of the Bonin high are sufficiently reproduced in hindcast simulations with that resolution as will be shown in Section 3. The details of the experimental design are given in each section showing simulation results.

### 3. Hindcast simulations

In this section, hindcast simulations from 15 July 2004 are described. Representation of observed features, such as propagation of Rossby waves and intensification of the Bonin high, heavy rain falls in Sakata and Fukui on 17–18 July and heat waves on 20 July 2004 are examined.

#### 3.1 Experimental design

Hindcast simulations were conducted for seven days from 0 UTC, 15 July 2004, 5-days prior to the heat wave in Tokyo. The initial conditions are prepared from those for JMA GSM (Global Spectral Model). The grid-point values (GPV) of GSM is provided with the horizontal resolution of  $1.25^\circ$  at 16 pressure levels (1000, 925, 850, 700, 500, 400, 300, 250, 200, 150, 100, 70, 50, 30, 20, 10 hPa). The

horizontal interpolation was conducted in the spectral space using SPHEREPACK (Adams and Swartrauber 1997). The surface pressure ( $p_s$ ) in GPV is not used but recalculated from the geopotential height ( $z$ ), temperature ( $T$ ) in GPV and the surface height ( $z_s$ ) of AFES in order to avoid unwanted waves due to the differences in the orography between GPV and AFES. Using the recalculated  $p_s$ , the horizontal winds ( $u, v$ ), and temperature ( $T$ ) are interpolated vertically to the model levels. The specific humidity ( $q$ ) is calculated from the relative humidity (RH),  $T$  and pressure ( $p$ ) at pressure levels and interpolated vertically to the model levels. The initial values of the cloud and ground water are set to naught.

The distribution of the sea-surface temperature (SST) and sea-ice concentration are prepared from the NCEP RTG (Real-time global) SST (Thébaux et al. 2003) and MMAB (the Marine Modeling and Analysis Branch) sea-ice analyses (Grumbine 1997), respectively. These SSTs and sea-ice data are provided daily at  $0.5^\circ$  in the horizontal. They are interpolated to the model grid points after a simple quality check for sea-ice.

#### 3.2 The Silk Road pattern and intensification on the Bonin high

At the initial time, a wave packet is located near  $30^\circ\text{E}$  (Fig. 6) and propagates eastward during the next several days. The major features of the propagation of a Rossby wave packet in the analysis (Fig. 8) are reproduced in the hindcast (Fig. 9), in particular, the simulated location of the equivalent-barotropic anticyclone ( $125^\circ\text{E}$ ,  $35^\circ\text{N}$ ) is very close to the analysis. Undulation of the northern margin of the Tibetan high implies the propagation of Rossby waves along the Asian jet in the upper-troposphere (Fig. 9a). Indeed the wave activity flux is reproduced well although the over-reflection process at jet entrance and exit is somewhat exaggerated as evidenced by larger arrows near  $60^\circ\text{E}$  and  $170^\circ\text{E}$ . In the calculation of the wave activity flux, the simulated perturbation components include model bias since the climatology of the NCEP/NCAR reanalysis is used as the basic fields in place of a long-term integration of the model due to prohibitive computational costs to obtain model climatology at a high resolution. Lower-tropospheric anticyclonic flows are correctly reproduced in the southwestern Japan and contribute to a realistic distribution of the out-going long-wave radiation (OLR, Fig. 9b).

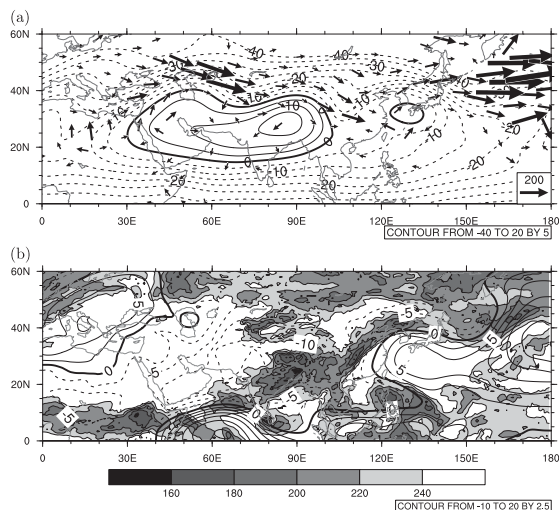


Fig. 9. Distributions of (a) the streamfunction ( $\times 10^6 \text{ m}^2 \text{ s}$ , contour) and wave activity flux ( $\text{m}^2 \text{ s}^{-2}$ , arrows) at the 200-hPa surface (b) the stream function ( $\times 10^6 \text{ m}^2 \text{ s}$ , contour) at the 850-hPa surface and outgoing long-wave radiation ( $\text{W m}^{-2}$ , shade) averaged in 17–21 July 2004 simulated by AFES using the T639L48 resolution from 0 UTC, 15 July.

### 3.3 Heavy rainfall in Sakata and Fukui

In this subsection, intense precipitation events in Sakata (A in Fig. 3) and Fukui ( $136^\circ\text{E}$ ,  $36^\circ\text{N}$ ), which occurred during 17–18 July about a few days prior to the heat wave event, are investigated in relation to the intensification of the Bonin high.

Figure 10 shows daily precipitation on 17 (Fig. 10a, c, e) and 18 July (Fig. 10b, d, f) produced from radar and surface (AMeDAS) observations (Fig. 10a, 10b), and moderate- (Fig. 10c, 10d) and high-resolution (Fig. 10e, 10f) simulations. In this section the local time (JST, UTF + 9) is used to examine changes in precipitation patterns between the two days. On 17 July, rainfalls are found over Tohoku and Hokuriku (between  $36^\circ\text{N}$  and  $40^\circ\text{N}$ ) including Sakata. As the Baiu frontal zone migrates southward, rainfalls are concentrated near Fukui on 18 July. These observed precipitation patterns are reproduced in simulations with both moderate and high resolutions. Similarities of precipitation patterns imply the role of clockwise synoptic-scale flows that bring moist air at low levels to maintain instabilities.

Simulated precipitation is, however, much less

than that from observation. Note that the contour intervals are halved for simulations. This is partly due to a rather simple precipitation scheme and an insufficient resolution to resolve cloud scales. The observed rainfalls in Fig. 10a, 10b are band-shaped (Kato and Aranami 2005), probably caused by latent instability (Yamasaki 2008) and maintained by the back-building mechanism (Taniwatari 2006). Such cloud- and meso-scale mechanisms are not represented in GCMs. Simulated precipitation is caused primarily in the convective parametrization at each column. It is speculated that the differences in precipitation mechanisms cause the different shapes of heavy precipitation.

On 17 July, counterparts of a few centres of precipitation in Tohoku (Fig. 10a) are also found in the high-resolution simulation (Fig. 10e) but not in the moderate resolution-simulation (Fig. 10c) although the overall pattern is slightly shifted northward in both simulations. On 18 July, although the Fukui rainfall (Fig. 10b) is reproduced at both resolutions (Fig. 10d, f), the simulated precipitation in the moderate-resolution simulation is very weak. These differences may be caused partly by the representation of orography and partly by the representation of flows, filaments of the potential temperature at low levels, in particular. Although the Japanese Alps near  $138^\circ\text{E}$ ,  $36^\circ\text{N}$  are represented in both resolutions, they are represented as a single peak at the moderate-resolution (about 83-km mesh). At the high-resolution (about 21-km mesh), several major mountain ranges are resolved (not shown). Figure 2 of Kitagawa (2008) compares orography of previous and current global numerical weather forecast models at JMA. Their horizontal resolutions (20 and 60 km) are similar to the ones in this paper.

Figure 11 presents the time evolution of the 850-hPa equivalent potential temperature at every 12 hour between 12 UTC 16 to 0 UTC 18 July. Figure 11a, c, e, g are produced from the analysis for the JMA's regional spectral model (RSM). The horizontal resolution of RSM is 20 km and that of the distributed data at pressure levels is  $0.5^\circ$  and  $0.4^\circ$  in the zonal and meridional directions. At 12 UTC on 16 July, a tongue with high potential temperature is extended eastward from southern China toward Japan. This moist tongue is associated with the Baiu/Meiyu frontal zone and the low-level flows of the subtropical anticyclone contribute to converging moisture from the south. The front is intensified as it migrates southward.

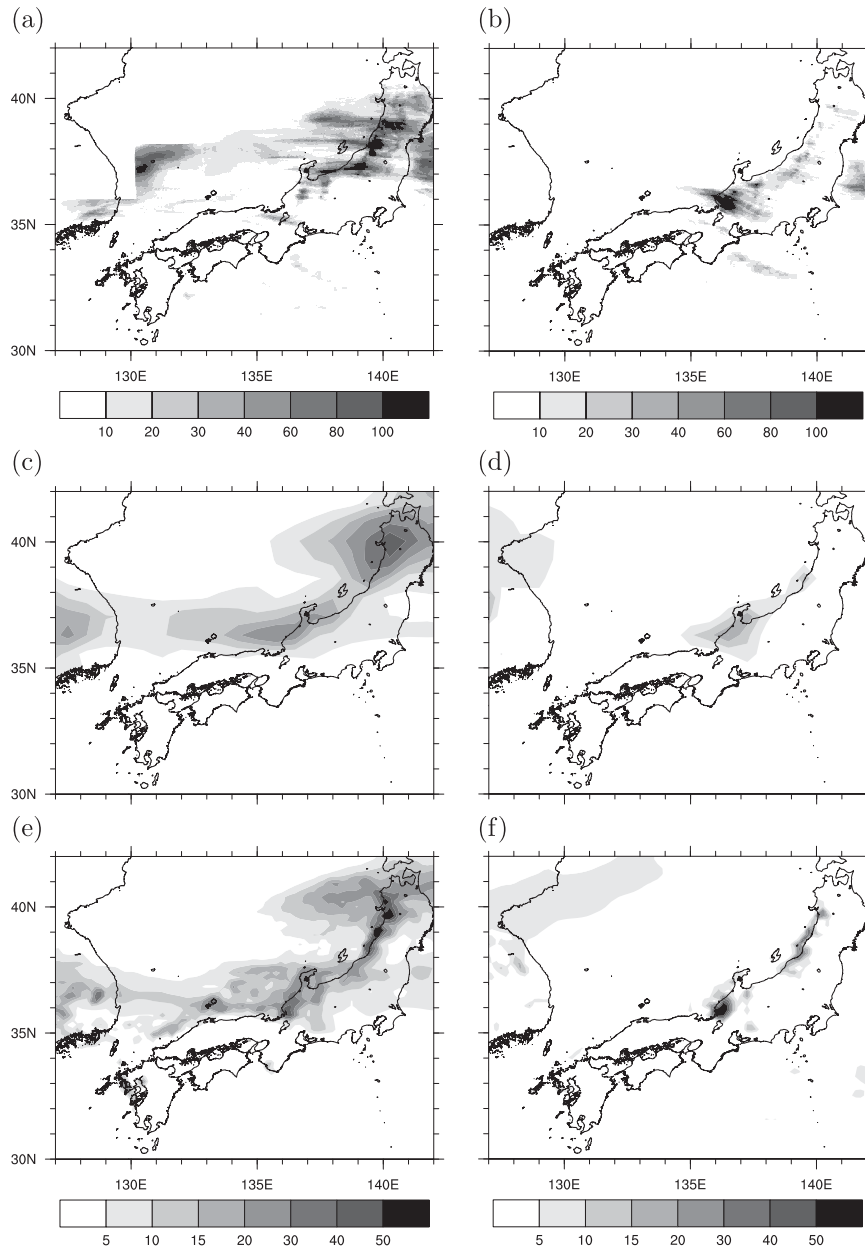


Fig. 10. Observed (Radar-AMeDAS, a, b) and simulated (moderate resolution, c, d; high resolution, e, f) daily precipitation ( $\text{mm d}^{-1}$ ) on 17 (a, c, e) and 18 (b, d, f) July 2004. Note that the shading intervals are halved for simulated precipitation.

The high-resolution simulation (Fig. 11b, d, f, h) reproduces these observed features. At 12 UTC on 17 and 0 UTC on 18 July, large equivalent potential temperature is advected eastward reaching the coast of the island of Honshu along the Sea of Japan. The frontogenesis is somewhat more intense in the simulation. Although the simulated moist

tongue is more convex northward than that of the analysis, the large equivalent potential temperature comes from the upstream of the anticyclonic flows in both analysis and simulation. The moderate-resolution simulation reproduces similar synoptic distributions but fine anomalous peaks are absent (not shown).

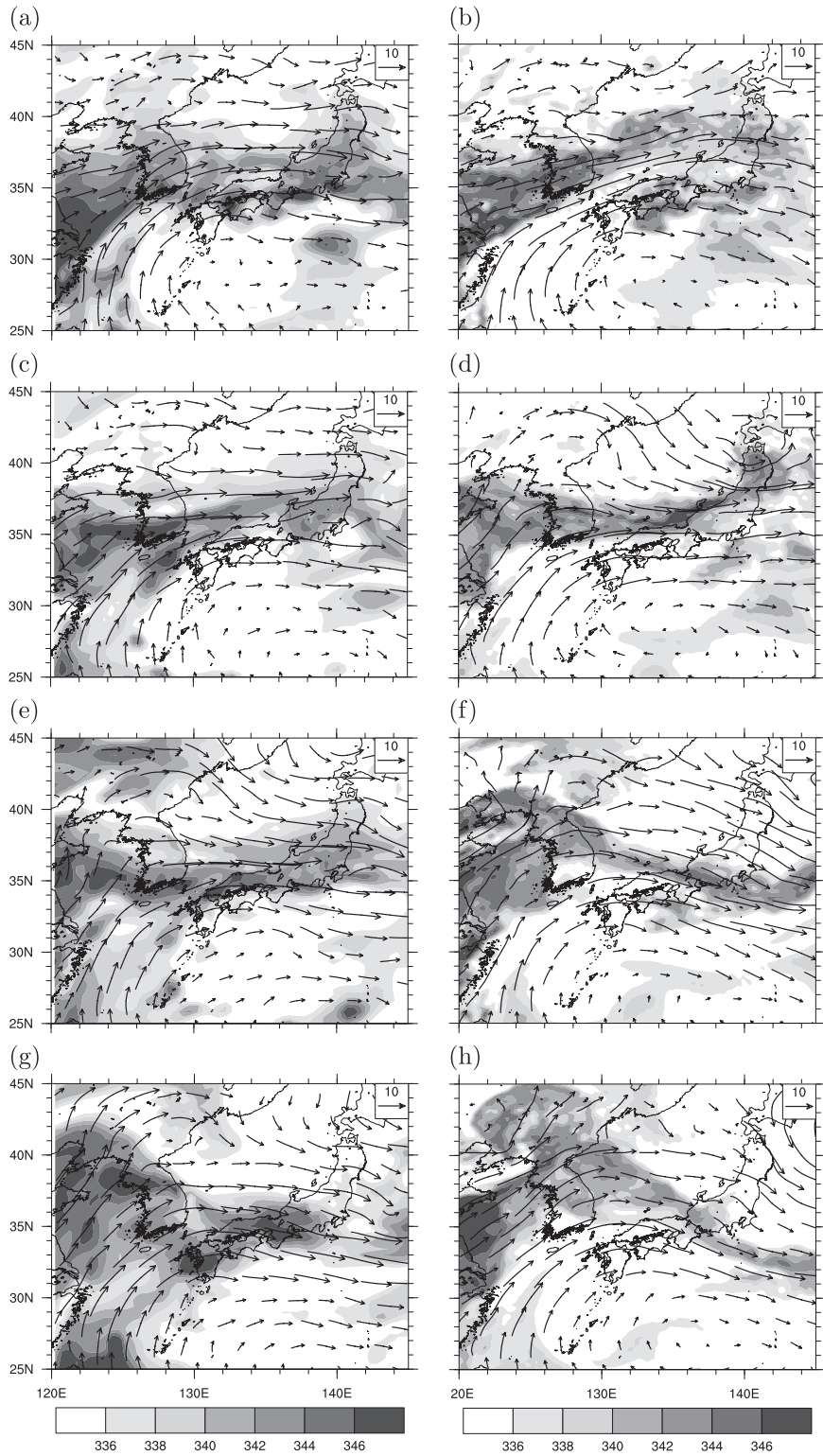


Fig. 11. Time evolution of the equivalent potential temperature (K) at 850 hPa from 12 UTC on 16 to 0 UTC 18 July 2004 drawn every 12 hours. Left and right columns are produced from the analysis (RSM) and AFES 21-km mesh simulation, respectively.

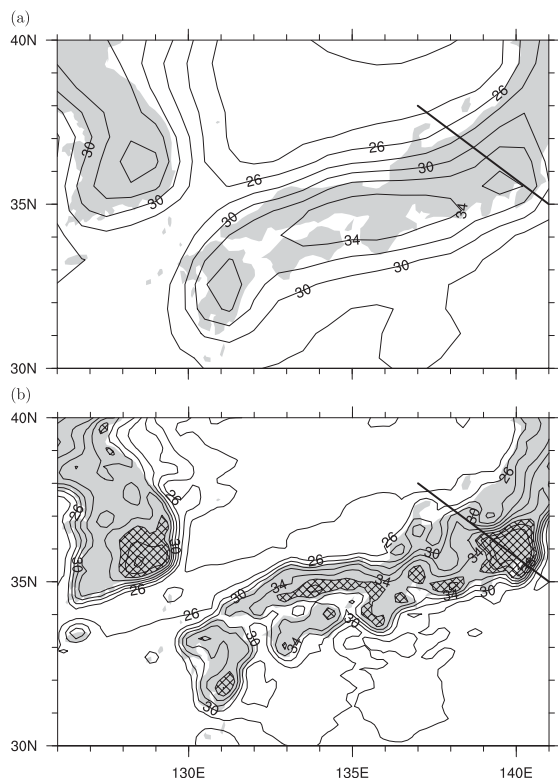


Fig. 12. Distribution of the 2-m temperature ( $^{\circ}\text{C}$ ) near Japan at 6 UTC on 20 July, 2004 in the (a) T159L48 (b) T639L48 hindcast from 0 UTC, 15 July. Contours are drawn every 2 degrees between 22 and 40 $^{\circ}\text{C}$  and regions with temperature higher than 36 $^{\circ}\text{C}$  are hatched. The solid line represents the transection in Fig. 13.

### 3.4 Heat wave in Tokyo

Figure 12 shows the simulated 2-m temperature at 6 UTC 20 July. The 2-m temperature is diagnosed from the temperatures on the surface and model's lowest level and bulk Richardson number in the surface flux calculation. In both moderate- (Fig. 12a) and high- (Fig. 12b) simulations, regions with warm temperature are located along the Pacific coast, or the lee side of the mountains. Similarities between the two simulations at different resolutions imply the dominance of the large-scale flows, such as the Silk Road pattern and intensification of the Bonin high, in the formation mechanisms of the heat wave.

In the high-resolution simulation (Fig. 12b) the simulated warm regions are more localized and reproducing the temperature distribution of the meso-scale analysis (Fig. 3). Note that slightly different contour levels are used between Fig. 3 and 12 in order to highlight the very warm regions. As discussed in Section 1, the meso-scale analysis underestimates temperature. The high-resolution simulation overestimates maxima. This warm bias may partly be attributable to the initial wetness of naught.

The temperature at 6 UTC (15 Japan Standard time) at some arbitrarily selected two lee- and several windward-side observational stations is summarized in Table 1. The values at the closest grid points are shown for the analysis and simulation. This is shown so as not to compare values at each site quantitatively but to supplement maps (Fig. 3 and 12) and to demonstrate the capability of the 5-day high-resolution hindcast to reproduce localized high temperature.

There are a few factors causing the föhn: 1) condensational heating on the windward side and dry

Table 1. Observed (AMeDAS), analysed (MSM) and simulated (AFES) temperature values at 6 UTC, 20 July 2004. Letters A–I are marked in Fig. 3.

|   | Station    | latitude $^{\circ}\text{N}$ | longitude $^{\circ}\text{E}$ | AMeDAS | MSM  | AFES |
|---|------------|-----------------------------|------------------------------|--------|------|------|
| A | Sakata     | 38.91                       | 139.84                       | 25.3   | 24.0 | 25.9 |
| B | Niigata    | 37.91                       | 139.05                       | 26.9   | 24.7 | 27.1 |
| C | Kumagaya   | 36.15                       | 139.38                       | 37.6   | 32.3 | 40.9 |
| D | Tokyo      | 35.69                       | 139.76                       | 37.4   | 34.5 | 41.2 |
| E | Ushiku     | 35.40                       | 140.15                       | 38.0   | 31.4 | 41.2 |
| F | Hamamatsu  | 34.71                       | 137.72                       | 35.0   | 31.8 | 40.9 |
| G | Shingu     | 33.69                       | 135.97                       | 34.6   | 32.8 | 40.2 |
| H | Okayama    | 34.66                       | 133.92                       | 34.9   | 32.4 | 38.9 |
| I | Nakamura   | 33.00                       | 132.92                       | 35.9   | 34.0 | 37.7 |
| J | Miyakonojo | 31.73                       | 131.08                       | 34.1   | 32.5 | 39.2 |

descent on the lee side of the mountains, 2) radiative heating, 3) folding down of isentropes (Ikawa and Nagasawa 1989). The Föhn due to the folded isentropes is adiabatic and often caused by mountain waves (Scorer and Klieforth 1959). The convective activity associated with the Baiu front produced diabatic heating on the windward side of the mountains. In fact, there is a notable contrast of humidity between the windward and lee sides of the mountains. The relative humidity is low (50–60%) where high temperature occurs. In spite of this, the moist process seems to be less important than the adiabatic process. Even if a parcel near the surface with 26°C were lifted to 1000 m with lapse rate of 4 K km<sup>-1</sup> and brought to the sea level with lapse rate of 10 K, the temperature would be 32°C. This is about 5 K less than observed values near Tokyo.

The transections of the potential temperature (Fig. 13) indicate the primary role of the adiabatic process. The contours below 800 hPa are violently meandered at both resolutions. Meanders are less significant in the moderate-resolution simulation (Fig. 13a) but higher temperature would be reproduced if the altitude on the lee side were lower. Undulation at upper levels in the high-resolution simulation (Fig. 13b) implies mountain waves. Almost vertical contours imply a well-mixed layer. Presumably radiative heating contributes to heating the surface to enhance mixing. The near-surface temperature is overestimated probably due to a lack of initial soil moisture. As a result, the dry adjustment might be overreacting. Undulation of the potential temperature surface is also found in the meso-scale analysis but it is less significant (not shown) in accordance with underestimated temperature maxima (Fig. 3 and Table 1).

Representation of the orography would explain the differences in localization of high temperature as in that of rainfalls (cf. Subsection 3.3). The peak of the mountain is lower and less localized in the moderate-resolution model (shades in Fig. 13). Moreover, the Kyushu, Shikoku, and Chugoku mountain ranges are replaced with a single mountain range with reduced height at the peaks (e.g. 796.8 and 246.3 m at the peak in the Kyushu mountain range in the high and moderate-resolution models, respectively). Thus a local maximum near Okayama (Letter 'H' in Fig. 3) cannot be reproduced with the moderate resolution. The föhn regions are indeed realistically localized along the lee side of each mountain range in the high-resolution simulation (Fig. 12b).

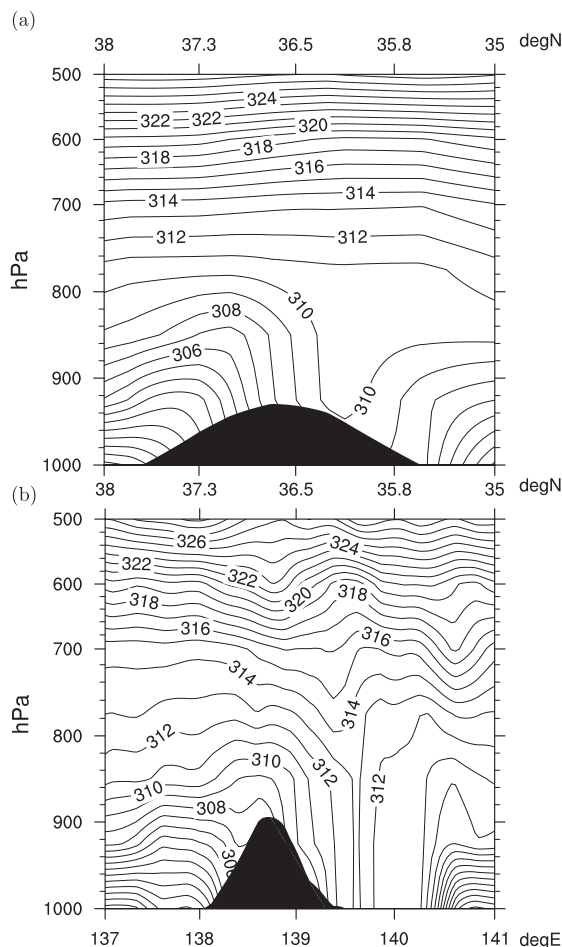


Fig. 13. Transection of potential temperature (K) between 137°E, 38°N and 141°E, 35°N used in (a) the moderate (T159, about 83-km mesh), (b) high (T639, about 21-km mesh) resolution runs. Contours are drawn every 1 K. The filled regions at the bottom represent the shape of the mountains.

#### 4. Ensemble experiments

Deterministic hindcast simulations imply a longer predictability of the Rossby-wave propagation and associated local weather events. In order to study the predictability of the propagation of Rossby-wave packets and monsoon variability, ensemble experiments were conducted.

##### 4.1 Experimental settings

A moderate horizontal resolution of T159L48 (about 83-km mesh) allows representation of the Silk Road pattern and intensification of the Bonin

Table 2. Differences in the sea-surface boundary conditions used in three ensemble experiments.

| experiment | sea-surface boundary conditions   |
|------------|-----------------------------------|
| control    | climatology                       |
| hindcast   | daily analysis                    |
| forecast   | climatology + anomalies on 1 July |

high (cf. Subsection 3.2). Although regional events and their feedback are not sufficiently resolved, potential for local high-impact events could be estimated from a moderate-resolution ensemble to some extent.

Initial ensemble perturbations of the JMA weekly ensemble forecast are used. Perturbations are generated using the breeding vector method (Toth and Kalnay 1993, Kyouda 2006). There are 25 members composed of the unperturbed control run, 12 modes and their sign reversed. The GPV of weekly forecast is provided at three pressure levels (850, 500, 300 hPa) for  $u$ ,  $v$ ,  $z$ ,  $T$ , RH at 850 hPa and surface variables at the horizontal resolution of  $2.5^\circ$ . Perturbations from the control are added to the initial condition as follows. The horizontal interpolation was performed in spectral space using SPHEREPACK. Perturbations at 850 hPa are also used for 1000 and 925 hPa. Perturbations at 700 and 400 hPa are interpolated from adjacent levels in log pressure coordinates. The perturbations between 250 and 70 hPa are damped towards 0 at 70 hPa.

Three ensemble experiments with different sea-surface boundary conditions were conducted to identify their impacts (Table 2). The control run uses the climatological values averaged between 1982 and 2004, prepared from the weekly NOAA Optimum Interpolation (OI) SST and sea-ice data (Reynolds et al. 2002). The daily values are interpolated in time from the weekly averages. The hindcast run uses the same RTG SST and MMAB sea-ice data as the hindcast simulations but for the period from 1 to 31 July 2004. The forecast run employs a technique commonly used in operational seasonal forecasts with AGCM. The anomalies on 1 July 2004 are fixed throughout the integration period and superimposed on the climatological time evolution in July. Thus SST and sea-ice distribution of the hindcast and forecast runs are identical at the initial time and gradually become different.

## 4.2 Results

In order to examine the predictability of the variability of the Tibetan anticyclone, attentions are focused upon the geopotential height at the 200-hPa level. One of the measures of forecast skills is the correlation of the forecast and analysis anomalies (anomaly correlation, AC) used in many previous studies (e.g. Miyakoda et al. 1986). The correlation is defined as

$$AC = \frac{xy}{\sqrt{x^2y^2}},$$

where  $x$  and  $y$  are the deviations. Figure 14 shows the 200 hPa geopotential height anomalies of the ensemble mean of the forecast run and NCEP/NCAR reanalysis from the climatology of the NCEP/NCAR reanalysis on 4, 7, 10 July 2004. The ensemble mean of  $n$  members is defined as

$$\bar{z} = \frac{1}{n} \sum_{i=1}^n z_i.$$

On 4 July, the analysis (Fig. 14a) and forecast (Fig. 14b) are very similar. The anomaly correlations in the Northern Hemisphere (NH) and the Silk Road region (SR,  $30^\circ\text{E}$ – $120^\circ\text{E}$ ,  $30^\circ\text{N}$ – $50^\circ\text{N}$ ) are 0.84 and 0.83, respectively. On 7 July, there are more discrepancies between the analysis (Fig. 14c) and (Fig. 14d). As a result, AC in NH reduces to be 0.59, marginally useful. In SR, by contrast, anomalies are still quite similar (AC = 0.70). On 10 July, there are not many similarities outside the Silk Road region (AC = 0.50 in NH and AC = 0.91 in SR). Although the amplitude is smaller than the analysis, a wave-like pattern in SR (Fig. 14e) is reproduced in the forecast (Fig. 14f).

The time evolution of the anomaly correlations of the ensemble mean of the three simulations is shown in Fig. 15, where anomalies are defined to be the difference from the long-time (1968–1996) average of the NCEP/NCAR reanalysis. The thick and thin curves are the averages in the Northern Hemisphere and in the Silk Road region. Anomaly correlations are larger than 0.6, i.e. accurate enough to be a useful forecast, for about 7 and 13 days in NH and SR, respectively. That is, SR has a longer predictability by 6 days. The maintenance, or even increase of the anomaly correlation around 10 July, might be partly due to the propagation of Rossby waves, whose signal is present at the initial time (Fig. 6 and 16a).

Differences in the boundary conditions do not

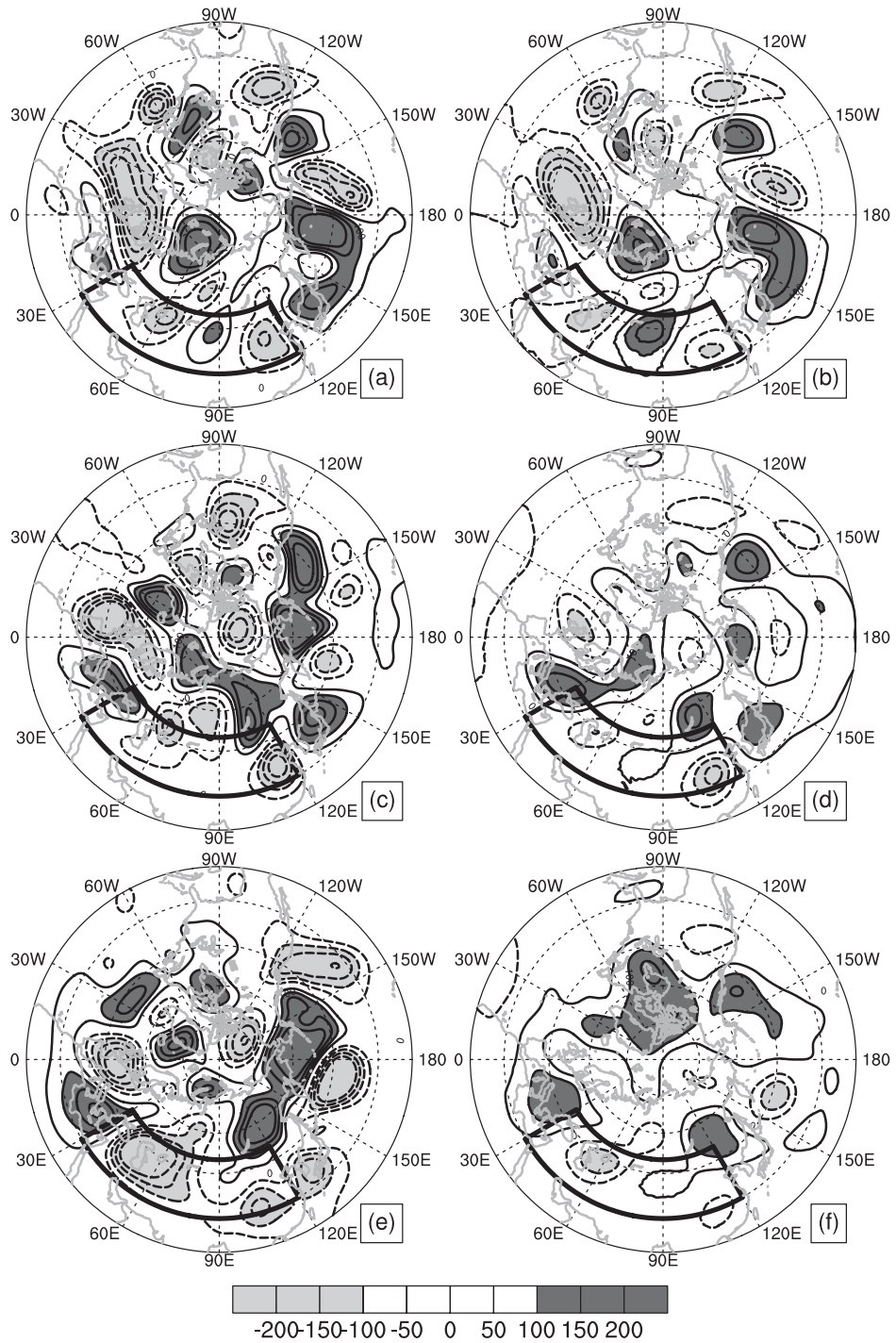


Fig. 14. Anomalies of the 200 hPa geopotential height (gpm) from the climatology of the NCEP/NCAR re-analysis on 4 (a, b), 7 (c, d), 10 (e, f) July 2004 in the NCEP/NCAR analysis (a, c, e) and ensemble mean of the AFES forecast (b, d, f). Anomalies smaller than  $-100$  gpm and larger than  $100$  gpm are light- and dark-shaded, respectively. Negative contours are broken. The Silk Road region ( $30^{\circ}\text{E}$ – $120^{\circ}\text{E}$ ,  $30^{\circ}\text{N}$ – $50^{\circ}\text{N}$ ) is designated by a rectangle.

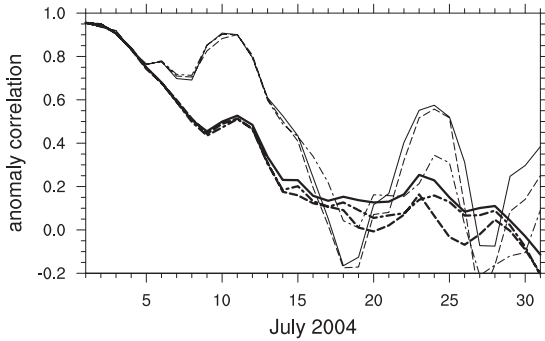


Fig. 15. Anomaly correlations of the 200-hPa geopotential height in the Northern Hemisphere in thick curves and in the Silk Road region (30°E–120°E, 30°N–50°N) in thin curves. The solid, broken and dot-dashed curves correspond to the forecast, control and hindcast experiments.

seem to be significant in the first two weeks but become gradually important in the latter half. However, imposing the analysed SST does not help the hindcast to outperform the other experiments. The differences among the experiments are further examined later in this section.

Figure 16a shows the longitude-time cross-section of the ensemble-mean geopotential height averaged between 35°N and 50°N at the 200-hPa level in the forecast experiment. The zonal average is removed for clarity. A Rossby-wave packet propagating from 90°E on 1 July to 15°W on 25 July (Fig. 6) is reproduced in the ensemble mean of the forecast. In addition, a few other wave packets are also discernible although they are not as clear as the first one. At 120°E, the positive anomaly that corresponds to the equivalent barotropic anticyclone near Japan modulates in time and has maxima in the middle and end of the month. It is suspected that the Rossby-wave propagation affects these modulations of the high.

These features found in the second and third week, even near the end of the month imply some predictability. Figure 16b shows the ensemble spread of the geopotential height at the 200-hPa level. Here the ensemble spread is defined as the ‘biased’ standard deviation (dividing the squared sum of anomalies by the number of ensemble members  $n$  in place of  $n - 1$ ),

$$s = \sqrt{\frac{1}{n} \sum_{i=1}^n (z_i - \bar{z})^2},$$

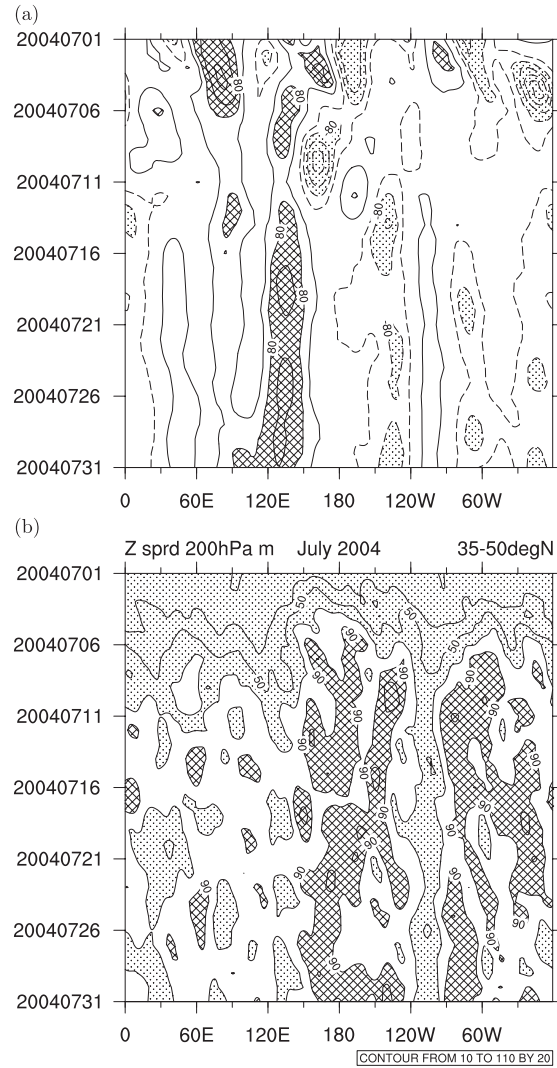


Fig. 16. Longitude-time cross-sections of (a) the ensemble-mean geopotential height anomaly from the zonal mean and (b) the ensemble spread of the geopotential height at the 200-hPa level average in 35°N and 50°N. Values smaller than –80 m (Panel a) and 70 m (Panel b) are dotted. Values larger than 80 m (Panel a) and 90 m (Panel b) are hatched.

where  $\bar{z}$  is the ensemble mean. In general, the ensemble members diverge less over the Eurasian and North American continent than over the Pacific and Atlantic. The smaller ensemble spread over the continent implies less error and hence a longer predictability. This asymmetry could be due to the difference in the initial error, growth between cy-

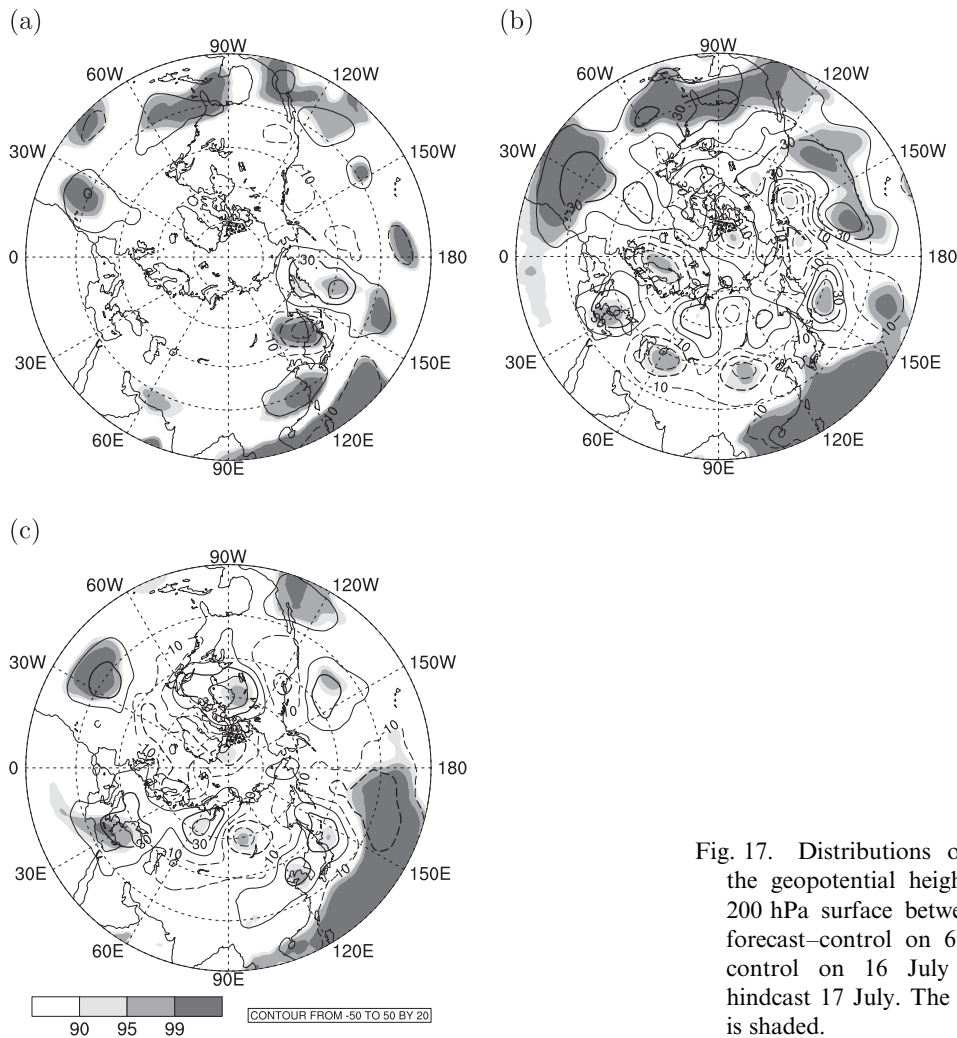


Fig. 17. Distributions of the difference of the geopotential height (contours) at the 200 hPa surface between experiments: (a) forecast-control on 6 July, (b) forecast-control on 16 July and (c) forecast-hindcast 17 July. The confidence level (%) is shaded.

clone and anticyclone, relative importance between diabatic and adiabatic processes and boundary conditions (land and ocean). In order to clarify causes of this asymmetry, a number of ensemble forecast experiments are required, which would be explored elsewhere.

It is interesting to note that the ensemble spread decreases as the ridge near Japan enhances. The smaller ensemble spread indicates more confidence on the enhancement of this ridge. It is implied that some events that were affected by Rossby waves, such as the Silk Road pattern and the enhancement of the equivalent-barotropic high near Japan, might have predictability beyond week two.

Finally, the differences between the ensemble means are examined in order to obtain insights into how the forecast error would propagate. Fig-

ure 17a and 17b show the differences of the ensemble mean geopotential height at the 200 hPa level between the forecast and control runs in contours. The anomalies with darker shades have larger confidence.

On 6 July, a train of errors is found between the western Pacific and Japan (Fig. 17a). This pattern resembles the Pacific-Japan pattern (Nitta 1987). Anomalies found near Japan and its east can be interpreted as propagation of Rossby waves. Negative (about  $-1$  K) and positive (about  $1-2$  K, not shown) SST anomalies in the Philippine and East China Seas are probably responsible for this pattern. On 16 July, anomalies reminiscent of the Silk Road pattern are found over the Eurasian continent (Fig. 17b). This pattern emerges in the decaying phase of an intensified anticyclonic anomaly

over the east Mediterranean Sea. These cases exemplify how the error is communicated over the globe.

The difference between the forecast and hindcast runs is small in the first two weeks. These two runs diverge in the latter half of the month. On 17 July, a train of errors, reminiscent of the propagation pattern causing the intensification of the Okhotsk anticyclone (Nakamura and Fukamachi 2004), is found over the northern Eurasia (Maeda et al. 2006). These differences appear to be emanating from the Barents Sea, where no significant SST anomaly from the climatology is found on 1 July but a positive SST anomaly ( $>2$  K) emerges on 16 July (not shown). Other locations with significant SST changes include the Mediterranean sea and the western Pacific to the east of Japan, where the warm anomalies existent at the initial time disappear about two weeks later.

Similarities between propagation of errors and Rossby waves suggest that the activity of Rossby waves is one of the important source of errors (Palmer and Tibaldi 1988). At the same time, it suggests the importance of these three propagation patterns upon the summer climate of East Asia.

## 5. Summary and discussion

Hindcast simulations were conducted to study these high-impact weather events in Japan in July 2004 (Fig. 1, 2, 3). Although these high-impact weather events themselves are usually in meso-scales, they are closely related to the larger scales (Fig. 5–7).

In the precipitation events in Sakata and Fukui (Fig. 10), an unstable region is created at the tip of the moist tongue (Fig. 11). Although the band-shaped precipitation cannot be resolved and the amount of precipitation is much less, the model has succeeded in reproducing almost the correct timings and locations of the environment that caused the events a few days in advance.

The heat wave in Tokyo on 20 July is reproduced surprisingly well in the 21-km mesh global hindcast simulation. The 5-day simulation not only captures the hemispheric propagation of Rossby waves (Fig. 8–9), but also the anomalous temperature distribution over Japan and the Korean Peninsula (Fig. 3, 12, Table 1). In addition to the accurate representation of the large-scale flow, which can be also reproduced at a lower resolution, the detailed orography in the high-resolution has allowed accurate temperature distribution of the föhn (Fig. 13).

Ensemble forecast experiments were performed

to investigate predictability of propagation of Rossby waves and associated weather events. It is found that the Silk Road region has as twice as long predictability as the entire Northern Hemisphere in the ensemble simulations from 1 July 2004 (Fig. 14, 15). It appears that the propagation of Rossby waves acts to maintain the accuracy. The modulation of the Bonin high seems to have some predictability beyond the second week (Fig. 16). No apparent evidence is found that indicates better performance of the hindcast using the analysed SST over the other two, the control run with the climatological SST and forecast with the initial anomaly superimposed on the climatological SST in the first two weeks (Fig. 15). However, the distribution of the anomalous SST can be quite different even within the week and the error due to the wrong SST anomalies propagates rapidly over the globe along the wave-guides (Fig. 17).

The case studies here suggest a few methods that might improve the prediction of high-impact weather. First, the use of a high resolution of 10–20 km is rewarding and promising since it has a capability of reproducing some meso-scale systems and a phenomenon affected by detailed topography. The output from the high-resolution global model would be better initial and boundary conditions for regional models. Dynamical downscaling with a regional model seems to be a practical tool to reproduce local phenomena that cannot be resolved by the global model. Second, considering that the propagation of Rossby waves tends to have a better predictability, it might be able to identify possible severe weather events. Basically, the propagation of a significant wave packet with a small ensemble spread implies some severe weather to occur. Sensitivity analysis using ensemble forecast may be conducted to obtain the initial perturbations that cause the high-impact weather in the verification region. Then, a forecast using a higher-resolution global or regional model with these perturbations is conducted to predict “the worst case scenario” (e.g. Enomoto et al. 2007).

In general, high-impact weather is likely to occur at the leading edge of the filamentary structure of near-surface equivalent potential temperature (“moist tongue”) or potential vorticity near the tropopause (“PV streamer”). The filamentary structure represents the link among a wide range of horizontal scales. Its width is narrow enough to be in the meso-scales and its extent is long enough to be in the large-scales. These filaments are often the

result of the propagation and breaking of Rossby waves at the large-scales and sometimes give birth to meso-scale systems. The high-impact weather events that occurred in July 2004 in Japan can be regarded as such global-to-regional phenomena.

### Acknowledgements

Useful comments from the two anonymous reviewers and editor Mr Hosaka (MRI, JMA) helped us improving the manuscript. Dr Wakatsuki (FRCGC, JAMSTEC) and Dr Yamane (Doshisha University) provided Fortran programs to process GPV and boundary conditions, respectively. The NCEP/NCAR reanalysis data is provided by the NOAA/OAR/ESRL PSD, Boulder, Colorado, USA, from their OPeNDAP server. The NCAR Command Language (NCL) was used for data processing and visualization. Computation is performed on the Earth Simulator. This work is partly supported by KAKENHI 17740317.

### References

- Adams, J. C., and P. N. Swarztrauber, 1997: SPHERE-PACK 2.0: A model development facility. *NCAR Tech. Note*, NCAR/TN-436-STR, 59pp.
- Arakawa, A., and M. J. Suarez, 1983: Vertical differencing of the primitive equations in sigma coordinates. *Mon. Wea. Rev.*, **111**, 34–45.
- Emanuel, K. A., 1991: A scheme for representing cumulus convection in large-scale models. *J. Atmos. Sci.*, **48**, 2313–2335.
- Emanuel, K. A., and M. Živković-Rothman, 1999: Development and evaluation of a convection scheme for use in climate models. *J. Atmos. Sci.*, **56**, 1766–1782.
- Enomoto, T., 2004: Interannual variability of the Bonin high associated with the propagation of Rossby waves along the Asian jet. *J. Meteor. Soc. Japan*, **82**, 1019–1034.
- Enomoto, T., B. J. Hoskins, and Y. Matsuda, 2003: The formation mechanism of the Bonin high in August. *Quart. J. Roy. Meteor. Soc.*, **587**, 157–178.
- Enomoto, T., W. Ohfuchi, H. Nakamura, and M. A. Shapiro, 2007: Remote effects of tropical storm Cristobal upon a cut-off cyclone over Europe in August 2002. *Meteor. Atmos. Phys.*, **96**, 29–42.
- Enomoto, T., A. Kuwano-Yoshida, N. Komori, and W. Ohfuchi, 2008: Description of AFES 2: Improvements for high-resolution and coupled simulations. *In High Resolution Numerical Modelling of the Atmosphere and Ocean*, K. Hamilton and W. Ohfuchi (eds.), chapter 5, pp. 77–97, Springer, New York.
- Grumbine, R. W., 1997: Automated passive microwave sea ice concentration analysis at NCEP. *Technical Procedures Bulletin*, **440**, National Weather Service, 13pp.
- Harada, Y., H. Endo, and T. Enomoto, 2006: Formation mechanism of the anticyclone that caused heat waves in Japan in July 2004. *Special issue on the variability of summer climate, Kaiyo Monthly*, **44**, 151–159, (in Japanese).
- Hoskins, B. J., and A. J. Simmons, 1975: A multi-layer spectral model and the semi-implicit method. *Quart. J. Roy. Meteor. Soc.*, **101**, 637–655.
- Ikawa, M., and Y. Nagasawa, 1989: A numerical study of a dynamically induced foehn observed in the Abashiri-Ohmu area. *J. Meteor. Soc. Japan*, **67**, 429–458.
- Kalnay, E., M. Kanamitsu, R. Kistler, W. Collins, D. Deaven, L. Gandin, M. Iredell, S. Saha, G. White, J. Woollen, Y. Zhu, A. Leetmaa, B. Reynolds, M. Chelliah, W. Ebisuzaki, W. Higgins, J. Janowiak, K. C. Mo, C. Ropelewski, J. Wang, R. Jenne, and D. Joseph, 1996: The NCEP/NCAR 40-Year Reanalysis Project. *Bull. Amer. Meteor. Soc.*, **77**, 437–471.
- Kato, T., and K. Aranami, 2005: Formation factors of 2004 Niigata-Fukushima and Fukui heavy rainfalls and problems in predictions using a cloud-resolving model. *SOLA*, **1**, 1–4, doi:10.2151/sola.2005-001.
- Kitagawa, H., 2008: A new high-resolution global numerical forecast model at JMA. *Tenki*, **55**, 509–514, (in Japanese).
- Kyouda, M., 2006: Chapter 3.1 The one-week ensemble prediction system. *In Introduction of Ensemble Technique to short- and medium-range forecasting—With the aim of the improvement in the forecast skill of extreme weather event—, Annual NPD/JMA report*, Separated Vol. **52**, 23–33.
- Le Treut, H., and Z. -X. Li, 1991: Sensitivity of an atmospheric general circulation model to prescribed SST changes: feedback effects associated with the simulation of cloud optical properties. *Climate Dyn.*, **5**, 175–187.
- Louis, J. -F., 1979: A parametric model of vertical eddy fluxes in the atmosphere. *Bound.-Layer Meteor.*, **17**, 187–202.
- Maeda, S., H. Sato, and A. Ito, 2006: One-month prediction of Okhotsk high in 2003/4 summer. *Special issue on the variability of summer climate, Kaiyo Monthly*, **44**, 24–31, (in Japanese).
- Mellor, G. L., and T. Yamada, 1982: Development of a turbulent closure model for geophysical fluid problems. *Rev. Geophys. Space Phys.*, **20**, 851–875.
- Miyakoda, K., J. Sirutis, and J. Ploshay, 1986: One-month forecast experiments—without anomaly boundary forcings. *Mon. Wea. Rev.*, **114**, 2363–2401.

- Nakajima, T., and M. Tanaka, 1986: Matrix formulation for the transfer of solar radiation in a plane-parallel scattering atmosphere. *J. Quart. Spectrosc. Radiat. Transfer*, **35**, 13–21.
- Nakajima, T., M. Tsukamoto, Y. Tsushima, A. Numaguti, and T. Kimura, 2000: Modeling of the radiative process in an atmospheric general circulation model. *Appl. Opt.*, **39**, 4869–4878.
- Nakamura, H., and T. Fukamachi, 2004: Evolution and dynamics of summertime blocking over the Far East and the associated surface Okhotsk high. *Quart. J. Roy. Meteor. Soc.*, **599**, 1213–1233.
- Nitta, T., 1987: Convective activities in the tropical western Pacific and their impact on the Northern Hemisphere summer circulation. *J. Meteor. Soc. Japan*, **65**, 373–390.
- Numaguti, A., M. Takahashi, T. Nakajima, and A. Sumi, 1997: Description of CCSR/NIES/Atmospheric General Circulation Model. *CGER's Supercomputer Monograph Report*, **3**, National Institute of Environmental Sciences, Tsukuba, Japan, pp. 1–48.
- Ohfuchi, W., H. Nakamura, M. K. Yoshioka, T. Enomoto, K. Takaya, X. Peng, S. Yamane, T. Nishimura, Y. Kurihara, and K. Ninomiya, 2004: 10-km mesh meso-scale resolving simulations of the global atmosphere on the Earth Simulator: Preliminary outcomes of AFES (AGCM for the Earth Simulator). *J. Earth Simulator*, **1**, 8–34.
- Palmer, T. N., and S. Tibaldi, 1988: On the prediction of forecast skill. *Mon. Wea. Rev.*, **116**, 2453–2480.
- Peng, M. S., J. A. Ridout, and T. F. Hogan, 2004: Recent modification of the Emanuel convective scheme in the Navy operational global atmospheric prediction system. *Mon. Wea. Rev.*, **132**, 1254–1268.
- Reynolds, R. W., N. A. Rayner, T. M. Smith, D. C. Stokes, and W. Wang, 2002: An improved in situ and satellite SST analysis for climate. *J. Climate*, **15**, 1609–1625.
- Rodwell, M. J., and B. J. Hoskins, 1996: Monsoons and the dynamics of deserts. *Quart. J. Roy. Meteor. Soc.*, **122**, 1385–1404.
- Sato, N., and M. Takahashi, 2006: Dynamical processes related to the appearance of quasi-stationary waves on the subtropical jet in the midsummer northern hemisphere. *J. Climate*, **19**, 1531–1544.
- Scorer, R. S., and H. Klieforth, 1959: Theory of mountain waves of large amplitude. *Quart. J. Roy. Meteor. Soc.*, **85**, 131–143.
- Shingu, S., H. Takahara, H. Fuchigami, M. Yamada, Y. Tsuda, W. Ohfuchi, Y. Sasaki, K. Kobayashi, T. Hagiwara, S. Habata, M. Yokokawa, H. Itoh, and K. Otsuka, 2002: A 26.58 Tflops global atmospheric simulation with the spectral transform method on the Earth Simulator. *Proceedings of Supercomputing 2002*, <http://www.sc-2002.org/paperpdfs/pap.pap331.pdf>.
- Shingu, S., H. Fuchigami, and M. Yamada, 2003: Vector parallel programming and performance of a spectral atmospheric model on the Earth Simulator. In *Realizing Teracomputing: Proceedings of the Tenth ECMWF Workshop on the Use of High Performance Computing in Meteorology*, W. Zwiefelhofer and N. Kreitz (Editors), 29–46, World Scientific.
- Smith, R. N. B., 1990: A scheme for predicting layer clouds and their water content in a general circulation model. *Quart. J. Roy. Meteor. Soc.*, **116**, 435–460.
- Sundqvist, H., 1978: A parametrization scheme for non-convective condensation including prediction of cloud water content. *Quart. J. Roy. Meteor. Soc.*, **104**, 677–690.
- Takaya, K., and H. Nakamura, 2001: A formulation of a phase-independent wave-activity flux for stationary and migratory quasigeostrophic eddies on a zonally varying basic flow. *J. Atmos., Sci.*, **58**, 608–627.
- Taniwatari, N., 2006: Analysis of torrential rainfalls in Fukui and overview of the associated damages. *Technical Reports of the Japan Meteorological Agency*, **129**, 56–65, (in Japanese).
- Thébaux, J., E. Rogers, W. Wang, and B. Katz, 2003: A new high-resolution blended real-time global sea surface temperature analysis. *Bull. Amer. Meteor. Soc.*, **84**, 645–656.
- Toth, Z., and E. Kalnay, 1993: Ensemble forecasting at NMC: the generation of perturbations. *Bull. Amer. Meteor. Soc.*, **74**, 2317–2330.
- Uno, I., X.-M. Cai, D. G. Steyn, and S. Emori, 1995: A simple extension of the Louis method for rough surface layer modelling. *Bound.-Layer Meteor.*, **76**, 395–409.
- Yamasaki, M., 2008: A study of Fukui heavy rainfall in 2004. *J. Meteor. Soc. Japan*, **86**, 369–376.